# $Gd^{3+}$-Functionalized Lithium Niobate Nanoparticles for Dual Multiphoton and Magnetic Resonance Bioimaging

*Raphaël De Matos,[1] Adrian Gheata,[1] Gabriel Campargue,[2] Jérémy Vuilleumier,[1] Laura Nicolle,[1] Katarzyna Pierzchala,[3] Ileana Jelescu,[4] Fiorella Lucarini,[5] Ivan Gautschi,[5] Florian Riporto,[6] Ronan Le Dantec,[6] Yannick Mugnier,[6] Anne-Sophie Chauvin,[7] Marinella Mazzanti,[7] Davide Staedler,[5] Dario Diviani,[5] Luigi Bonacina,[2] Sandrine Gerber-Lemaire[1]**

[1]Institute of Chemical Sciences and Engineering, Ecole Polytechnique Fédérale de Lausanne, Group for Functionalized Biomaterials, EPFL SB ISIC SCI-SB-SG, Station 6, CH-1015 Lausanne, Switzerland

[2]Department of Applied Physics, Université de Genève, 22 Chemin de Pinchat, 1211 Genève 4, Switzerland

[3]Laboratory of Functional and Metabolic Imaging, Ecole Polytechnique Fédérale de Lausanne, CH-1015 Lausanne, Switzerland and Neurometabolic Unit, Service of Clinical Chemistry, University Hospital of Lausanne, CH-1011 Lausanne, Switzerland

[4]Animal Imaging and Technology, Center for Biomedical Imaging, EPFL, CH-1015 Lausanne, Switzerland

[5]Faculty of Biology and Medicine, Department of Biomedical Sciences, Université de Lausanne, CH-1011 Lausanne, Switzerland

[6]Université Savoie Mont-Blanc, SYMME, F-74000 Annecy, France

[7]Institute of Chemical Sciences and Engineering, Ecole Polytechnique Fédérale de Lausanne, Group of Coordination Chemistry, EPFL SB ISIC SCI-SB-MM, Station 6, CH-1015 Lausanne, Switzerland

KEYWORDS. Dual imaging modality, multiphoton microscopy, MRI $T_1$ contrast agents, surface functionalization, harmonic generation, dielectric nanoparticles.

ABSTRACT

Harmonic nanoparticles (HNPs) emerged as appealing exogenous probes for optical bio-imaging due to their distinctive features such as long-term photostability and spectral flexibility, allowing multiphoton excitation in the classical (NIR-I) and extended near infrared spectral windows (NIR-II and III). However, like all other optical labels, HNPs are not suitable for whole body imaging applications. In this work, we developed a bimodal nonlinear optical/magnetic resonance imaging (MRI) contrast agent through the covalent conjugation of Gd(III) chelates to coated lithium niobate (LNO) HNPs. We show that the resulting nanoconjugates exert strong contrast both in $T_1$ weighted MRI of agarose gel-based phantoms and in cancer cells by second harmonic generation upon excitation in the NIR region. Their capabilities for dual $T_1/T_2$ MRI was also emphasized by quantitative mapping of the phantom in both modes. The functionalization protocol ensured high stability of the Gd-functionalized HNPs in physiological environment and provided high $r_1$

relaxivity value per NP ($5.20x10^5$ $mM^{-1}s^{-1}$) while preserving their efficient nonlinear optical response.

## INTRODUCTION

Cellular[1] and immunocellular therapies[2] are rightfully listed among the most promising biomedical approaches for the years to come. The translation of these techniques to clinical practice requires the careful assessment of the fate of a selected cell population in the host organism. Tracking these cells individually poses several challenges in terms of sensitivity, selectivity, spatial resolution, penetration depth, and monitoring time-span.[3] While the use of exogenous probes can greatly improve sensitivity and contrast[4] in comparison to the signal from endogenous structures, none of the available imaging techniques can simultaneously provide (sub)cellular spatial resolution and whole body imaging capabilities, hence the idea pursued by several research groups to develop dual agents capable to exert contrast by different physical mechanisms. The range of techniques that can be exploited include magnetic resonance imaging (MRI), computed tomography (CT), ultrasound, photo-acoustic, luminescence imaging, linear and nonlinear microscopy.[5] MRI has virtually no limitation in terms of penetration depth and it does not involve ionizing radiation. On the down side, its spatial resolution in the order of tens of micrometers greatly exceeds the cell dimensions. On the opposite end of the spectrum, confocal optical microscopy provides sub-micron resolution in the three dimensions, but considerably poorer sample penetration (hundreds of micrometers). Multiphoton microscopy stands for an interesting alternative, as the longer wavelengths used for excitation suffer less from tissue scattering. Recently, thanks to the advent of new laser sources covering the second and third near-infrared windows[6] (NIR-II and III, alternatively referred to as short-wave-infrared-region (SWIR)), penetration depths of the order of

a millimeter have been reported.[7] One drawback associated with the use of SWIR excitation is related to the limited number of optical probes responding in this spectral region.[8,9]

Multifunctional nanoparticles (NPs) attracted a growing interest over the past decade for the development of multimodal probes for both *in vitro* and *in vivo* bioimaging and theranostic applications.[10-17] Owing to high agent loading ability and their surface properties which allow for tailored chemical modifications, inorganic NPs emerged as excellent candidates for engineering multimodal probes. Seminal achievements were reported with lanthanide-doped upconversion NPs for the combination of NIR luminescence imaging with complementary MRI, x-ray CT or positron emission tomography (PET) imaging modalities.[18-22] Nanoconjugates based on iron oxide NPs were also disclosed for dual MRI/PET and MRI/CT tumor imaging.[23,24] Due to their ultrasmall size and luminescence properties, noble metal nanoclusters were conjugated to gadolinium (Gd) ions to provide hybrid nanoprobes for targeted triple-modal NIR fluorescence / MRI / CT *in vivo* tumor imaging.[25,26] In addition to their multimodal imaging capabilities, nanoparticulate systems were used to increase the local concentration and efficiency of Gd-based MRI contrast agents by providing an effective delivery of reporters and a high payload of paramagnetic ions to target sites.[27-31] Recently, harmonic NPs (HNPs) were proposed as highly efficient NIR probes presenting several complementary advantages with respect to other optically active NPs,[32-34] including the flexibility of the excitation wavelength, the absence of saturation, bleaching/blinking events[35] and the possibility to colocalize the simultaneously emitted second and third harmonic signals excited for their identification in optically complex environment such as tumor tissues.[36] We previously demonstrated the potential of bismuth ferrite ($BiFeO_3$) HNPs for cell labeling and tracking by NIR-II multiphoton microscopy in both muscle and lung tissue.[37,38] Sugiyama et al. reported the labeling of hematopoietic stem cells with low concentrations of barium titanate

($BaTiO_3$) HNPs to understand their cellular uptake and intracellular fate,[39] and other authors demonstrated their *in vivo* application.[40,41] The inherent flexibility and stability of the nonlinear response of HNPs upon excitation from UV to NIR-II,[33] NIR-III[42] and NIR-IV[42] would be highly advantageous in the context of multimodal imaging combining their capability for nonlinear optical response with magnetic properties for MRI. Recently, the surface decoration of $BaTiO_3$ HNPs with gold or silver nanoparticles allowed for combined two-photon second harmonic generation imaging and one-photon surface enhanced Raman scattering in living cells.[43]

Herein, we disclose the first nanoconjugate based on a lithium niobate ($LiNbO_3$, LNO) harmonic core[44] functionalized with chelated $Gd^{3+}$ ions for bimodal optical/MR bioimaging. The conjugation strategy made use of copper-catalyzed [3+2] cycloaddition (click reaction) at the surface of silica-coated LNO HNPs with a terminal alkyne-modified analogue of the tripodal propionate ligand $H_3$ebpatcn.[45] First, we assessed the nonlinear optical imaging properties of the resulting $Gd^{3+}$-functionalized LNO HNPs upon incubation with DU145 human prostate cancer cells. Successively, we studied the longitudinal and transverse relaxation rates of water protons in the presence of these nanoconjugates at 30 and 60 MHz, followed by calculation of their proton relaxivities. Further investigation of their ability to be used as dual $T_1$-$T_2$ contrast agent included single phantom experiments at 9.4 T NMR spectrometer and 14.1 T MRI quantitative $T_1$ and $T_2$ mapping, which demonstrated the capability of Gd-conjugated LNO HNPs to act as bimodal MRI contrast agent and efficient optical markers for multi-harmonic imaging.

## EXPERIMENTAL SECTION

**Electron microscopy**. High angle annular dark field-scanning transmission electron microscopy (HAADF-STEM) images were acquired on a FEI Tecnai Osiris at 200 kV, using the following

parameters: probe 0.8 nA, collection angle 10 mrad, CL 115 mm. Energy dispersive X-ray (EDX) spectroscopy elemental maps were acquired on a FEI Tecnai Osiris, using a super-X detector. Samples were prepared by drop-casting colloidal suspension of **LNO-Gd** NPs on thin amorphous carbon films (Electron Microscopy Sciences).

**X-ray photoelectron spectroscopy (XPS) analysis**. Measurements were carried out on a Phi VersaProbe II (Physical Electronics Inc., MN, USA) using the monochromated *K*α X-ray line of an aluminium anode (1486.6eV) operated at ~50W. The XPS spectra acquisition was performed according to the parameters previously described.[46] Details on the calculation of surface atomic concentrations are given in Supporting Information (S-20), Table S1.

**Cell imaging**. 150'000 DU145 human prostate cancer cells were seeded in 29 mm glass-bottom dishes (Cellvis, D29-20-1.5-N) using RPMI 1640 medium supplemented with GlutaMAXTM (GIBCO N◦61870036), non-essential amino acids (GIBCO N◦1140035), 10% heat-inactivated fetal bovine serum (FBS)(GIBCO N◦10270106), and gentamycin (100µg/mL)(GIBCO N◦15750045). Cell layers were then washed once with phosphate-buffered saline (PBS) and treated with **LNO-Gd** NPs (50 µg/mL) in medium. After 48 h incubation, cell layers were washed twice with PBS, fixed for 20 minutes using 4% paraformaldehyde (PFA) and finally stained with DAPI (Roth, 6335.1) (1:5000) for 30 minutes.

A Leica SP8 Dive Falcon upright multiphoton microscope coupled with an Insight X3 tunable femtosecond laser (Newport Spectra-Physics) was used to acquire multiphoton images of the fixed cells. The laser was focused onto the sample by a Leica HC FLUOTAR L 25x/0.95 water immersion objective. The epi-collected signals were separated within tailored spectral ranges using the Leica 4Tune system and detected by a photomultiplier and a hybrid detector. We proceeded by

first acquiring simultaneously the THG and SHG channels upon excitation at 1250 nm and successively the SHG and DAPI channels upon 800 nm excitation.

**Relaxation measurements**. The analyses were performed on permanent magnets (Bruker Minispec spectrometers) with proton frequencies at 30 MHz (0.7 T) and 60 MHz (1.4 T). **LNO**, **LNO-N$_3$** or **LNO-Gd** NPs were suspended in $H_2O$ (600 μL, 2mg/mL), in 5 mm NMR tubes and ultrasonicated for 30 min. The complex **8** was dissolved in $H_2O$ (600 μL, 1.36 mM), in a 5 mm NMR tube. The samples were loaded in the spectrometer and the temperature was stabilized at 37°C for 15 min. The longitudinal relaxation time ($T_1$) was measured with inversion recovery method and the transverse relaxation time ($T_2$) was measured with CPMG spin echo sequence. All measurements correspond to an average over 4 scans. The acquisition parameters were adapted from ref. 46 and are given in Supporting Information (S-21).

The relaxation rate $R$i ($s^{-1}$) were calculated using equation (1):

$$R_i = \frac{1}{T_i} \qquad (1)$$

The relaxivity values ($mM^{-1}s^{-1}$) were calculated using equation (2):

$$r_i = \frac{\frac{1}{T_i} - \frac{1}{T_{id}}}{c} \qquad (2)$$

($i$=1 the longitudinal relaxation and $i$=2 the transverse relaxation of water in presence of the paramagnetic relaxing agent, $c$ = concentration of paramagnetic species [mM]). $T_{id}$ stands for the longitudinal or transverse relaxation of pure deionized water protons. The concentration of Gd(III) ions was determined by ICP-MS analysis (NexIon 350D, Perkin Elmer). $T_i$, $R_i$ and $r_i$ values are detailed in Supporting information (S-21, S-22).

**Agarose phantom relaxation measurements and MR imaging**. **LNO-Gd** NPs (suspended in water, 2 mg/mL) were mixed to a transparent solution of agarose (1.5%) in PBS (pH = 7.4, 144 mg/L $KH_2PO_4$, 9000 mg/L NaCl, 795 mg/L $Na_2HPO_4.7H_2O$) at 10 different concentrations: 1.50, 1.25, 1.00, 0.75, 0.50, 0.25, 0.20, 0.15, 0.10 and 0.00 mg/mL, and transferred into 5 mm NMR tubes. $T_1$ and $T_2$ relaxation constants were measured at 37°C and 9.4 T (400 MHz for $^1H$) on a Bruker spectrometer equipped with AVNeo console and 5mm BBI probe, using saturation recovery and cpmg sequences. To avoid relaxation damping during saturation due to high $^1H$ concentration, the probe was slightly detuned. The variable $T_1$ relaxation delays were set to 0.001, 0.010, 0.050, 0.075, 0.100, 0.250, 0.500, 0.750, 2.5, 5, 10, 25 s. The relaxation times $T_1$ were extracted, fitting the data with a monoexponential build-up. The $T_2$ echo delay was set to 2 ms and the variable cpmg loop counters were set to 2, 4, 6, 8, 10, 12, 16, 24, 32, 48, 64, 128. The relaxation times $T_2$ were extracted, fitting the data with a monoexponential decay. For MRI, the NMR tubes were then inserted into the homemade teflon NMR tube holder phantom. MRI experiments were performed on a 14.1 T Bruker Avance Neo system using ParaVision 360 software (Bruker BioSpin, D). A RAPID Biomedical GmbH volume coil was used for transmission and reception. 2D $T_1$ and $T_2$-weighted contrast images were collected using a gradient-echo sequence/fast low angle shot (FLASH) with the following parameters: $T_1$ - TE/TR = 2.75/500 ms, flip angle = 45°, $T_2$ - TE/TR = 12/5000 ms, flip angle = 136.42°, matrix size = 186 x 186, FOV = 27.9 x 27.9 $mm^2$, 9 axial 1-mm slices, 1 average. The repetition time (TR) was chosen to yield good contrast between the different samples at 14.1 T, based on the $T_1$ and $T_2$ relaxation time range measured at 9.4 T.

**Synthesis protocols**. Designation of the compounds refers to the chemical structures presented in Scheme 1 and Scheme 2. Chemicals (Aldrich, Acros, Fluka, Sigma, Maybridge, TCI Chemicals,

Apollo, abcr and Fluorochem) and reagent-grade solvents (Fluka, Riedel-de-Haën) were used without further purification. All reactions were performed in flame-dried glassware under an inert atmosphere. Completion of the reactions was monitored by thin layer chromatography (TLC) on pre-coated aluminum plates. Purifications were performed by flash column chromatography (FCC) on silica gel (Merck N° 9385 silica gel 60, 230-400 mesh, particle size 40-63 μm) or by dialysis against water at rt using dialysis tubes X12 Float-A-Lyzer G2 CE (10 mL, exclusion limit 100-500 Da). Lyophilizations were performed in a VaCo 5 freeze dryer (Zirbus, 0.3 mbar, -80°C). NMR and IR analyses, as well as accurate mass determination were performed according to the operating protocols previously described.[47]

*Preparation of compound* **3**.

A solution of pent-4-ynoic acid (3.00 g, 30.58 mmol, 1.0 eq.) and *N*-hydroxysuccinimide (3.52 g, 30.58 mmol, 1.0 eq.) in dry THF (100 mL) was cooled to 0 °C. DCC (6.31 g, 30.58 mmol, 1.0 eq.) dissolved in dry THF (35 mL) was added dropwise and the mixture was stirred at 0 °C for 45 min. The mixture was warmed to rt and stirred for 2 h. The mixture was filtered and concentrated under reduced pressure. The residue was dissolved in EtOAc (100 mL) and filtered to discard non-soluble residues. The filtrate was washed with a saturated aqueous solution of $NaHCO_3$ (100 mL) and brine (100 mL), dried over $MgSO_4$, filtered and concentrated under reduced pressure to afford 2,5-dioxopyrrolidin-1-yl pent-4-ynoate as a white solid (28.7 mmol, 5.60 g) This intermediate (3.00 g, 15.2 mmol, 1.0 eq.) was added dropwise to a solution of (*S*)-(−)-α-amino-γ-butyrolactone hydrobromide (**2**, 3.04 g, 16.72 mmol, 1.1 eq.) and $NEt_3$ (6.3 mL, 45.6 mmol, 3.0 eq.) in dry DCM (130 mL). The solution was stirred at rt for 2 h. The reaction mixture was washed with a saturated aqueous solution of $NH_4Cl$ (100 mL). The aqueous layer was extracted with DCM (100 mL, 8

times). The combined organic layers were dried over $MgSO_4$, filtered and concentrated under reduced pressure. The crude product was purified by FCC (PE/EtOAc 1:3) to afford **3** as a white solid (2.56 g, 14.0 mmol, 86% over 2 steps). The NMR data were in accordance with previously reported structures.[46] $^1$H-NMR spectrum (Supporting Information S-8).

*Preparation of compound* **4**. To a solution of **3** (500 mg, 2.76 mmol, 1.0 eq.) in MeOH (3 mL) was added conc. $H_2SO_4$ (cat., 5 drops) and the mixture was stirred at rt for 24 h. The mixture was cooled to 0 °C and the reaction was neutralized by addition of $NaHCO_3$ (until pH 7). The mixture was filtered and concentrated under reduced pressure at rt to afford methyl pent-4-ynoyl-*L*-homoserinate (600 mg, 2.76 mmol) which was used in the oxidation step without further purification. A solution of $(COCl)_2$ (0.24 mL, 2.76 mmol, 2.0 eq.) in dry DCM (8 mL) was cooled to -78 °C. DMSO (0.39 mL, 5.52 mmol, 4.0 eq.) in dry DCM (4 mL) was added dropwise and the mixture was stirred at -78 °C for 10 min. Methyl pent-4-ynoyl-*L*-homoserinate (294 mg, 1.38 mmol, 1.0 eq.) in dry DCM (4 mL) was added dropwise and the mixture was stirred at -78 °C for 30 min. $Et_3N$ (1.15 mL, 8.28 mmol, 6.0 eq.) was added dropwise and the mixture was warmed to 0 °C and stirred for 2 h. $H_2O$ (10 mL) was added and the aqueous layer was extracted with DCM (10 mL, 8 times). The combined organic layers were dried over $MgSO_4$, filtered and concentrated under reduced pressure. The crude product was purified by FCC (PE/EtOAc 1:3) to afford **4** as a yellow oil (126 mg, 0.60 mmol, 43%). $^1$H NMR (400 MHz, Chloroform-d) δ 9.71 (s, 1H), 6.56 (d, $J$ = 7.7 Hz, 1H), 4.87 (dt, $J$ = 7.8, 4.6 Hz, 1H), 3.75 (s, 3H), 3.17 (ddd, $J$ = 18.7, 4.8, 0.7 Hz, 1H), 3.12 – 3.04 (m, 1H), 2.56 – 2.38 (m, 4H), 1.99 (t, $J$ = 2.5 Hz, 1H). $^{13}$C NMR (101 MHz, Chloroform-d) δ 199.5, 171.2, 170.9, 82.7, 69.7, 53.0, 47.4, 45.7, 35.2, 14.9. HRMS (ESI/QTOF): *m/z* calcd for $C_{10}H_{14}NO_4^+$ ($[M + H]^+$): 212.0917; Found 212.0921. $^1$H-NMR, $^{13}$C-NMR spectra, IR data (Supporting Information S-8).

*Preparation of compound* **6**. To a solution of **5** (50 mg, 0.11 mmol, 1.0 eq.) in DCE/ACN dry (2:1, 0.6 mL) the L-homoserine derivative **4** (47 mg, 0.22 mmol, 2.0 eq.) in DCE/MeCN (2:1, 0.6 mL) was added dropwise followed by $NaBH_3CN$ (35 mg, 0.55 mmol, 5.0 eq) and the mixture was stirred at rt for 16 h. A saturated aqueous solution of $NaHCO_3$ (5 mL) was added and the aqueous layer was extracted with DCM (2 mL, 8 times). The combined organic layers were dried over $MgSO_4$, filtered and concentrated under reduced pressure. The crude product was purified by FCC ($Al_2O_3$ basic III (4.9 % water) DCM/MeOH 1:0 then 50:1) to afford the product as a yellow oil (27 mg, 0.05 mmol, 38 %). $^1$H NMR (400 MHz, Acetonitrile-$d_3$) δ 7.93 (dd, J = 7.6, 1.2 Hz, 2H), 7.86 (t, J = 7.7 Hz, 2H), 7.73 (d, J = 7.7 Hz, 2H), 7.20 (s, 1H), 4.49 (td, *J* = 8.0, 4.6 Hz, 1H), 4.36 (q, *J* = 7.1 Hz, 4H), 3.86 (s, 4H), 3.64 (s, 3H), 2.93 – 2.71 (m, 12H), 2.60 – 2.51 (m, 2H), 2.46 – 2.32 (m, 4H), 2.19 – 2.15 (m, 2H), 1.82 – 1.78 (m, 1H), 1.36 (t, *J* = 7.1 Hz, 6H). $^{13}$C NMR (101 MHz, Acetonitrile-$d_3$) δ 174.1, 171.8, 166.2, 148.6, 138.4, 127.5, 126.4, 124.2, 84.3, 70.1, 65.2, 62.3, 56.4, 54.5, 52.6, 52.0, 35.3, 26.3, 15.1, 14.6. HRMS (nanochip-ESI/LTQ-Orbitrap): m/z calcd for $C_{34}H_{47}N_6O_7^+$ ($[M + H]^+$): 651.3501; Found 651.3510. $^1$H-NMR, $^{13}$C-NMR spectra, IR data (Supporting Information S-10).

*Preparation of compound* **7**. To a solution of **6** (10 mg, 15 μmol, 1.0 eq.) in MeOH/$H_2O$ (5:1, 1.0 mL), LiOH (1.2 mg, 50 μmol, 3.3 eq.) was added and the mixture was stirred at rt for 3 h. The reaction mixture was diluted with $H_2O$ (2 mL) and washed with DCM (2 mL). The aqueous phase was then neutralized with HCl 1M. The resulting solution was transferred to a dialysis tube (MWCO 0.5 kDa) and dialyzed against water for 3 days. Lyophilization afforded **7** as a yellow solid (7.5 mg, 12 μmol, 83%). $^1$H NMR (400 MHz, Water-$d_2$): δ 7.85 (t, *J* = 7.80 Hz, 2H), 7.69 (m, 2H), 7.35 (m, 2H), 4.46 (s, 4H), 4.13 (dd, *J* = 7.9, 5.0 Hz, 1H), 3.68 (m, 12H), 3.37 (ddd, *J* =

30.4, 12.0, 4.9 Hz, 2H), 2.48 (m, 6H), 2.27 (s, 1H). $^{13}$C NMR (100 MHz, Water-$d_2$): δ 174.86, 174.10, 170.05, 151.16, 139.72, 125.51, 123.84, 70.01, 59.42, 54.62, 50-52, 34.23, 26.77, 14.36. HRMS (nanochip-ESI/LTQ-Orbitrap): m/z calcd for $C_{29}H_{38}N_6O_7^+$ ($[M + H]^+$): 582.2796; Found 582.2791. $^1$H-NMR, $^{13}$C-NMR spectra (Supporting Information S-11).

*Preparation of Gd chelate* **8**. To a solution of **7** (10 mg, 16 μmol, 1.0 eq) in $H_2O$ (500 μL) was added $GdCl_3 \cdot 6\ H_2O$ (6.3 mg, 17 μmol, 1.1 eq.) and the mixture was stirred at 37 °C for 16 h. The pH of the reaction mixture was maintained at 7.0 by addition of an aqueous solution of $NH_4OH$ (0.1M). The resulting solution was transferred to a dialysis tube (MWCO 0.5 kDa) and dialyzed against water for 3 days. Lyophilization afforded **8** as a yellow solid (13 mg, 16 μmol, quant.). HRMS (ESI/QTOF): *m/z* calcd for $C_{29}H_{33}GdN_6NaO_7^+$ ($[M + Na]^+$): 758.1544; Found 758.1549.

*Preparation of **LNO-Gd** NPs*. The surface functionalization protocol for the conjugation of **8** to **LNO-$N_3$** NPs was adapted from ref. 47, using copper-catalyzed [3+2] cycloaddition with the following quantities: **LNO-$N_3$** NPs (2 mg), **8** (0.76 mg, 1 μmol, 1.0 eq.), copper (II) sulfate (0.5 equiv, 0.5 μmol, 80 μg), sodium ascorbate (1.5 equiv, 1.5 μmol, 0.3 mg) in a mixture EtOH:$H_2O$ (1 mL:1.5 mL). The resulting **LNO-Gd** NPs were stored in distilled water (2 mg/mL) at 4°C.

## RESULTS AND DISCUSSION

**Synthesis of the chelating ligand and Gd(III) complexation**.

Tripodal picolinate ligands based on a 1,4,7-triazacyclononane (TACN) core were reported as efficient chelators for Gd(III) ions, leading to favorable relaxivity for MRI applications[45,48] and remarkable contrast efficiency in nanosized formulations.[27,28] The design of the chelating unit to be conjugated to the surface of HNPs made use of the previously reported disubstituted TACN

derivative **5**[45] (synthesis protocols detailed in Supporting Information, S-3) for Gd(III) coordination (Scheme 1). The L-homoserine analogue **4** was synthesized from (*S*)-(-)-α-amino-γ-butyrolactone (**2**) by coupling with pentynoic acid, followed by nucleophilic ring opening and subsequent Swern oxidation of the resulting highly sensitive primary alcohol. Reductive amination on the secondary amine of the TACN core delivered the protected chelating ligand **6**, presenting eight coordination moieties and a terminal alkyne for click reaction at the surface of HNPs. Saponification in the presence of LiOH, followed by dialysis against water delivered the Gd(III) chelator **7** in good yield. Subsequent reaction with $GdCl_3$ led to the Gd(III)-containing complex **8** for further conjugation to imaging NPs.

**Scheme 1**. Synthesis of TACN-Gd derivative **8** to be conjugated to LNO HNPs.

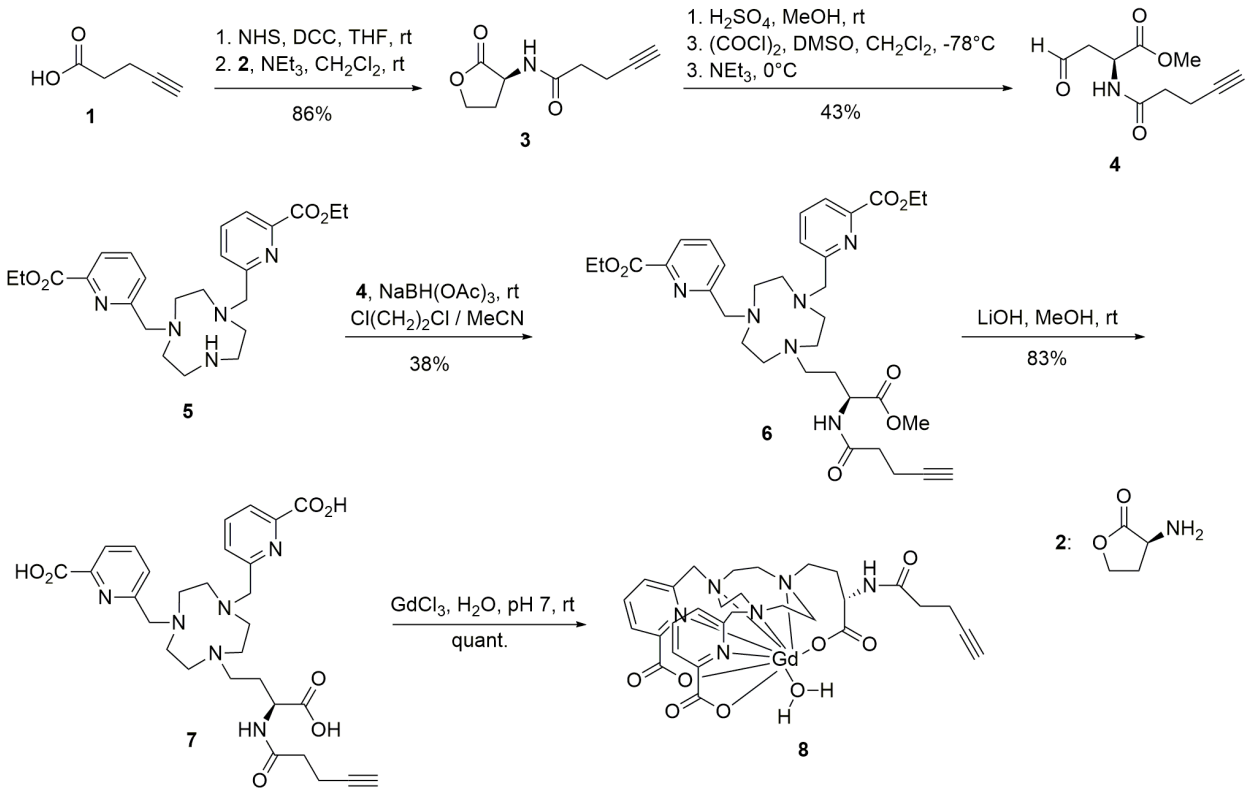

**Coating and functionalization of LNO HNPs**.

Surface modification of LNO HNPs (prepared by a non-aqueous solvothermal route from alkoxides;[44] for TEM images, see Supporting Information, Figure S1) followed the coating procedure established in our group for surface silanization of metal oxide HNPs.[47] A suspension of azido-modified NPs (**LNO-$N_3$**, coating procedure detailed in Supporting Information S-19) was ultrasonicated in the presence of the complex **8**, $CuSO_4$ and sodium ascorbate for 16 h, followed by repetitive cycles of centrifugation (10 min, 4'700 rpm) and washings ($H_2O$, 3 times) to discard unreacted ligand and reagents (Scheme 2). The resulting conjugates (**LNO-Gd**) were suspended in distilled water (2 mg/mL) for further characterization. During the functionalization process, the mean hydrodynamic diameter of the HNPs increased from 61.9 ± 4.4 nm (bare **LNO** NPs) to 157 ± 4.7 nm (**LNO-$N_3$**) and 153 ± 11 nm (**LNO-Gd**), while the zeta potential value shifted from -39.03 ± 0.99 mV (bare **LNO** NPs) to 22.07 ± 0.09 mV (**LNO-$N_3$**) and -8.59 ± 0.33 mV (**LNO-Gd**).

**Scheme 2**. Conjugation of Gd(III) complex to the surface of silanized LNO HNPs through copper-catalyzed [3+2] cycloaddition.

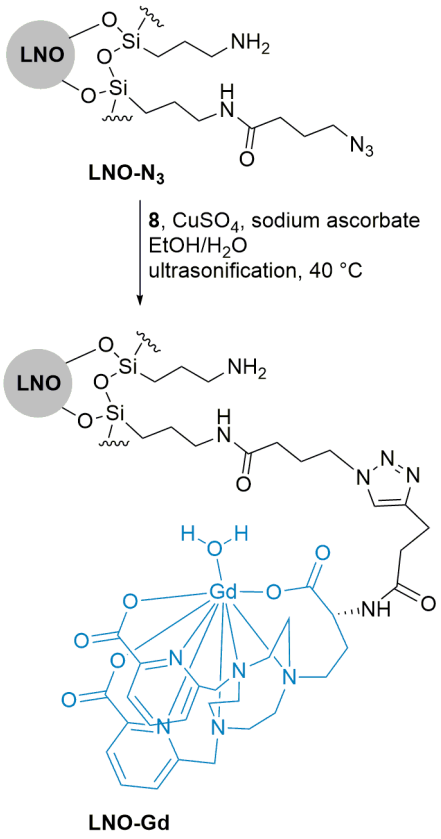


Further analysis by scanning transmission electron microscopy (STEM) and energy-dispersive X-ray (EDX) spectroscopy is presented in Figure 1A (for a representative image of an ensemble of functionalized NPs, see Supporting Information Figure S2). The Si EDX map gave evidence for efficient silanization of the core NPs which led to the formation of a dense coating layer averaging 10 nm thickness. Homogeneous distribution of the Gd(III)-containing complexes at the NP surface was confirmed in the Gd EDX map and merged elemental maps. The conjugation protocol resulted in up to $8x10^4$ chelates per NP (see Supporting Information S-22 for the calculation of the Gd(III) loading). X-ray photoelectron spectroscopy (XPS) was used to probe and determine the Gd atomic concentration at the surface of **LNO-Gd** NPs, which was measured at 0.62% relative to the other surface elements (Figure 1B; see Supporting Information, Figure S3 for survey, Table S1 for measured surface atomic concentrations). In addition, this study revealed that traces of copper

were efficiently removed from the samples of functionalized HNPs as the peak for Cu2p could not be measured within the detection limit of the analysis.

**Figure 1**. Characterization of **LNO-Gd** NPs. (A) Representative STEM images. Upper row: HAADF-STEM image, Nb EDX map; Medium row: Si EDX map, Gd EDX map; Lower row: Nb, Si and Gd EDX maps; scale bar: 50 nm. (B) XPS measurements. Multiplexes of the Gd3d peak from **LNO-N$_3$** NPs (blue) and **LNO-Gd** NPs (red).

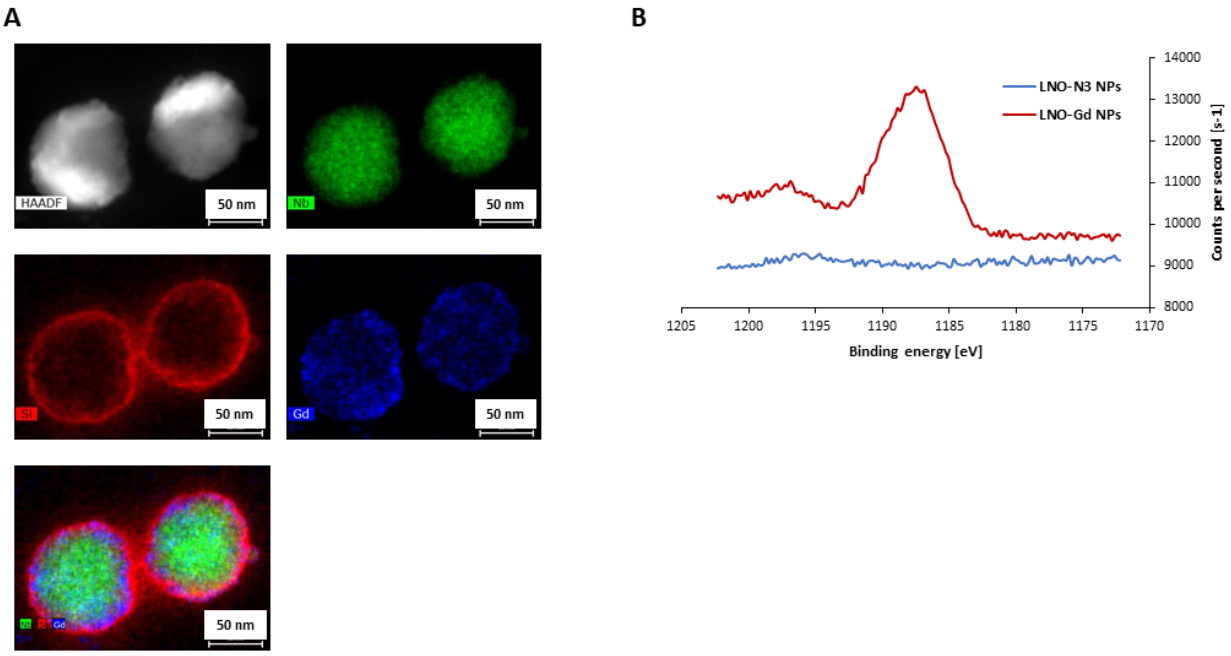


**Nonlinear optical imaging of LNO-Gd NPs**

The nonlinear response of LNO NPs upon femtosecond pulse excitation was first reported at 800 nm (SHG)[49] and successively in the 700-1300 nm excitation range for SHG[50] as well as for other non-linear and frequency mixing processes.[51] Very recently, SHG and THG from Mg-doped LNO NPs have been observed with excitation up to 2.2 μm.[42] At 800 nm, the SHG efficiency of the LNO NPs studied here was determined from ensemble measurements leading to an orientation-

averaged second-order susceptibility $\langle \chi^{(2)} \rangle$ value of ~40 pm/V.[52] In Figure 2, we present a complete set of multiphoton images obtained on DU145 human prostate cancer cells treated with **LNO-Gd** NPs at 50 µg/mL following the protocol reported in the experimental section. The image series was selected to highlight: i) the emission tunability, ii) the multi-order response, iii) the narrow spectral-bandwidth of the harmonic signals, and iv) the labeling properties of the nano-probes presented in this work. Each panel label reports the excitation wavelength, along with the attribution of the signal (*e.g.*, SHG @800 nm) and the spectral width of the corresponding detection channel. The SHG response is observed upon excitation at 800 and 1250 nm (i), SHG and THG are simultaneously detected upon 1250 nm excitation (ii), while under the same excitation, detection, and image plotting settings barely any signal is visible within an adjacent non-overlapping spectral range of the same width (iii). The DAPI channel allows identifying the cells present in the field of view. Although labeling is quite sparse, the nanoparticles outline the morphology of most cells displaying clearly their avoidance of the nuclear region (iv). We note that the labelling is not homogeneous for all cells: some of the cells in the left part of the image are labelled more faintly than the central ones.

Differently for the case of other materials,[53] we have not performed yet a thorough bio-assessment of the interaction between LNO nanoparticle and cells. Recently, Li *et al.* have studied the intra-cellular localization of LNO particles in mesenchymal stem cells within the size range used in our work and with a similar labeling protocol and particle concentration.[54] They reported that LNO NPs were internalized and accumulated preferentially in the perinuclear region and provided a concentration-dependent cytocompatibility assessment for this cell line.

**Figure 2**. Set of multiphoton images obtained on DU145 human prostate cancer treated with **LNO-Gd** NPs at 50 µg/mL. On each panel the labels indicates the signal attribution (THG, SHG,…), the excitation wavelength (800 or 1250 nm), and the spectral range for channel acquisition. Panels labelled CTRL are control images acquired and plotted using the same settings of the corresponding THG and SHG images excited at 1250 nm to highlight the narrow bandwidth of the harmonic emission. Scale bar: 20 µm.

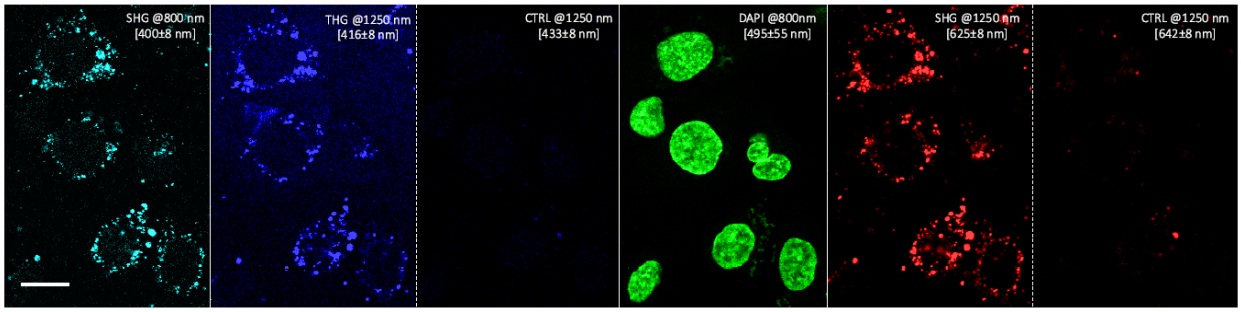


**Proton relaxivity of LNO-Gd NPs**

To assess the ability of **LNO-Gd** NPs to be used as MRI contrast agents, the longitudinal and transverse relaxation rates ($R_1$ and $R_2$, respectively) of their monohydrated complex were measured at 60 MHz (1.4 T), at physiological temperature (37°C) (Table 1; see Supporting Information for $T_i$ values and additional measurements at 30 MHz, S-21). The calculated relaxivity values of **8** and **LNO-Gd** NPs, on a per millimolar $Gd^{3+}$-ion basis, were compared to the characteristics reported for ebpatcn-Gd chelate,[45] marketed Gd-chelates[55] (Magnevist®, Multihance®, $r_i$ measured at 1.5 T) and small polymer coated gadolinium oxide NPs[56] (Dextran-SPGO, $r_i$ measured at 7.05 T). The $r_2/r_1$ ratio of the Gd(III)-chelate **8** is 1.1, which is consistent with the values reported for common low molecular weight Gd(III)-based $T_1$ contrast agents used in MRI bioimaging. Conjugation of this complex to the surface of LNO NPs led to a $r_2/r_1$ ratio of 2.4 for the resulting **LNO-Gd** NPs. Based on the Gd content, the relaxivity values $r_1$, in the presence **8** or **LNO-Gd** NPs, are similar

(6.92 and 6.35 $mM^{-1}s^{-1}$, respectively) indicating that the Gd(III) chelates at the NP surface adopt similar behavior as the species in solution. Such observation was previously disclosed on gold nanoconjugates[57] and multilayered assemblies of Gd(III) chelates on silica NPs.[58] Due to the high loading rate of chelate **8** to the NP surface, an estimated $r_1$ value of $5.20x10^5$ $mM^{-1}\cdot s^{-1}$ was reached for **LNO-Gd** NPs, on a per particle basis, which encouraged us to further evaluate their potential as contrast agents for $T_1$-weighted MRI.

**Table 1**. Relaxometric characteristics of complex **8**, functionalized LNO NPs (37°C, 1.4 T) and marketed Gd-chelate based contrast agents in water.

| | $R_1$ ($s^{-1}$) | $R_2$ ($s^{-1}$) | $r_1$ ($mM^{-1}s^{-1}$) | $r_2$ ($mM^{-1}s^{-1}$) |
|---|---|---|---|---|
| **8** | 9.68 | 11.24 | 6.92 | 7.74 |
| **LNO** NPs | 0.26 | 0.63 | - | - |
| **LNO-$N_3$** NPs | 0.29 | 0.89 | - | - |
| **LNO-Gd** NPs[a] | 4.52 | 10.68 | 6.35 | 15 |
| **LNO-Gd** NPs[b] | | | $5.20x10^5$ | $12.3x10^5$ |
| Gd(ebpatcn)($D_2O$) | | | 4.68[c] | 5.69[c] |
| Magnevist® | - | - | 3.3[d] | 3.9[d] |
| Multihance® | - | - | 4.0[d] | 4.3[d] |
| Dextran-SPGO ($Gd_2O_3$ core) | | | 4.8[e] | 16.9[e] |

[a]Relaxivities calculated per Gd(III) chelate; [b]Relaxivities estimated per NP; [c]Relaxivities measured at 1.05 T, 25°C from ref. 45; [d]Relaxivities measured at 1.5 T, from ref. 55; [e]Relaxivities measured at 7.05 T, from ref. 56.

**Evaluation of LNO-Gd NPs as $T_1$ and $T_2$ contrast agents**

Nowadays, most of the MRI scanners used for clinical diagnosis operate at high magnetic field strengths (> 1.5 T),[59] in particular those employed for whole body human imaging applications. Therefore, the properties of **LNO-Gd** NPs for contrast enhancement were investigated at 9.4 and 14.1 T. A commonly used agarose gel-based phantom[60,61] was designed and composed of eleven NMR tubes (5 mm diameter) with different concentrations of **LNO-Gd** NPs (Table 2, Figure 3A). A single phantom experiment was performed at 9.4 T NMR spectrometer to evaluate the $T_1$ spin-lattice and $T_2$ spin–spin relaxation times for increasing NPs concentrations (0.-1.5 mg/mL) (Figure 3B and 3C). A clear concentration-dependent enhancement of $R_1$ relaxation rate and shortening of $T_1$ relaxation time was observed over the studied concentration range, suggesting a signal-increasing imaging effect of **LNO-Gd** NPs. The $T_2$ relaxation time also decreased as the **LNO-Gd** NPs concentration increased, suggesting a decrease of signal-intensity as concentration of NPs increase.

**Table 2**. Composition of the agarose gel-based phantom.

| **Sample** | 1 | 2 | 3 | 4 | 5 | 6 | 7 | 8 | 9 | 10 | 11 |
|---|---|---|---|---|---|---|---|---|---|---|---|
| **LNO-Gd NPs concentration (mg/mL)** | 0.00 | 0.05 | 0.01 | 0.15 | 0.20 | 0.25 | 0.50 | 0.75 | 1.00 | 1.25 | 1.50 |

**Figure 3**. (A) Agarose gel-based phantom. (B) $T_1$ relaxation time and $R_1$ relaxation rate curves and (C) $T_2$ relaxation time and $R_2$ relaxation rate curves for **LNO-Gd** NPs concentrations of 0 - 1.5 mg/mL, at 9.4 T.

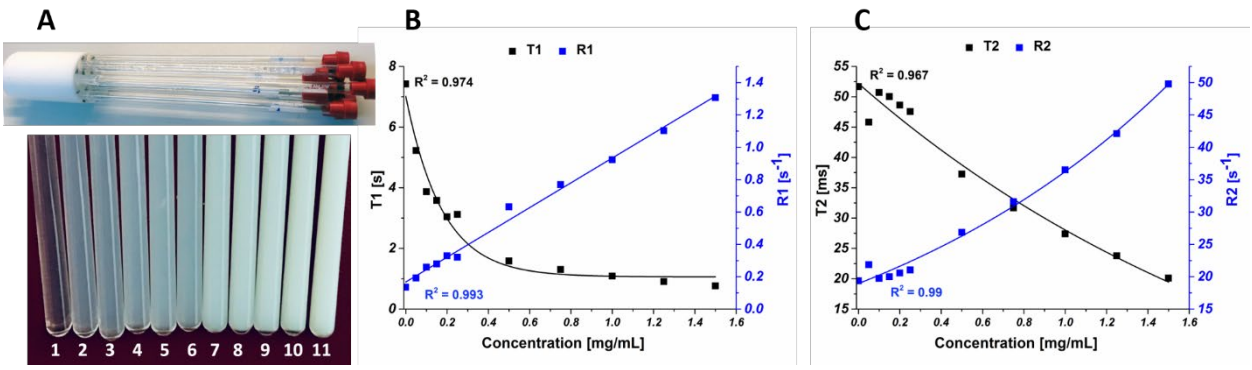


2D $T_1$-and $T_2$ weighted images of the phantom were collected using a gradient-echo sequence/fast low-angle shot (FLASH) on a 14.1 T MRI system (Figure 4A and 4D), highlighting a concentration-dependent increase of the signal intensity for $T_1$ weighted images and a significant signal decrease for $T_2$ weighted images. In addition, quantitative $T_1$ mapping of the phantom demonstrated statistically significant ($p<0.0001$) contrast enhancement correlated with **LNO-Gd** NPs concentrations (Figure 4B, 4C), while the $T_2$ mapping revealed a statistically significant ($p<0.0001$) contrast reduction (Figure 4E, 4F).

**Figure 4**. MR phantom images and contrast quantification at 14.1 T. (A) 2D $T_1$-weighted and (D) 2D $T_2$-weighted contrast image of the columnar phantom, FOV = 27.9 x 27.9 $mm^2$. (B) and (E) Contrast quantification curve. (C) Pearson correlation between $T_1$ relaxation time and $T_1$-weighted contrast enhancement and (F) Pearson correlation between $T_2$ relaxation time and $T_2$-weighted contrast enhancement related to the **LNO-Gd** NPs concentrations increase.

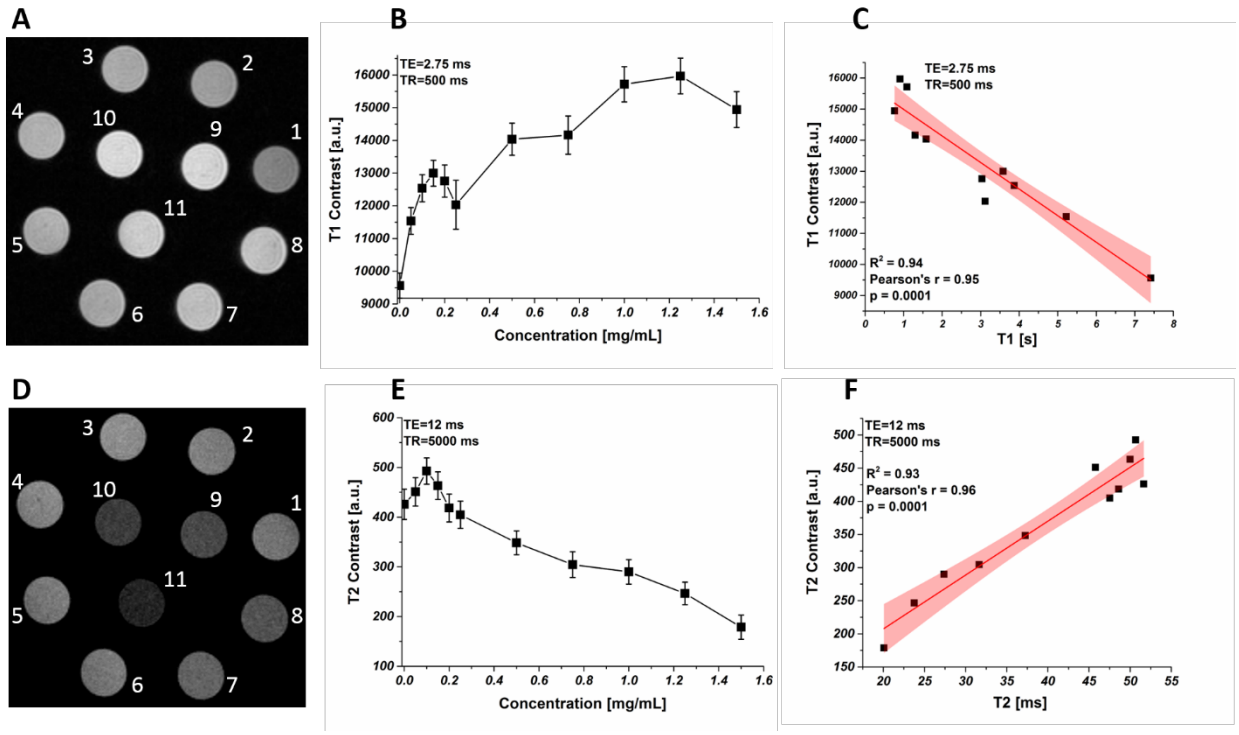


Most of the NP-based contrast agents used in clinics rely on superparamagnetic iron oxide (SPIO) materials which provide a strong contrast enhancement in $T_2$-weighted images, resulting in a signal-decreasing effect. Several limitations were reported for $T_2$ contrast agents, including the risk to confuse their dark signal with pathogenic lesions and their high susceptibility which is responsible for distortion of the magnetic field on neighboring healthy tissues, so-called the susceptibility artefact.[62] Despite their strong capacity for positive contrast enhancement, $T_1$ contrast agents based on low molecular weight Gd(III) chelates suffer from short circulation time *in vivo*, thus hampering MR images acquisition over long scan times. The development of NP-based contrast agents, combining $T_1/T_2$ dual mode contrast efficiencies, appears as an appealing strategy to achieve unequivocal detection of malignant lesions and improve the MRI diagnosis sensitivity.[63,64] Recent reports disclosed the possibility to turn SPIO NPs into $T_1/T_2$ dual mode contrast agents by modulation of the size and shape of the metal oxide core.[63,65] The combined loading of SPIO NPs and $Fe^{3+}$ or $Gd^{3+}$ chelates[66,67] into mesoporous nanomaterials showed high

potential for the targeted $T_1$-$T_2$ MRI of tumor tissues. The **LNO-Gd** nanoconjugates herein presented show a strong contrast enhancement in $T_1$-weighted images, resulting from the homogeneous dispersion and high payload of $Gd^{3+}$ chelates at their surface. Noteworthy, comparison of the relaxivity values ($r_1$) at 1.4 T of **LNO-Gd** NPs with commercial contrast agents suggest that excellent contrast should be obtained in short acquisition times on clinical MRI systems which generally operate at 3 and 7 T. Their capacity for contrast reduction in $T_2$ imaging mode was also demonstrated. In addition, the labeling and efficient imaging of DU145 human prostate cancer cells was achieved by the same conjugates, thanks to the intense SHG signal of the inorganic core upon excitation at 810 nm. We also verified that the relaxometric properties of **LNO-Gd** NPs remained unchanged after the excitation conditions applied for multiphoton imaging, indicating the stability of the surface conjugation to $Gd^{3+}$ chelates.

## CONCLUSIONS

Surface coated LNO HNPs conjugated to Gd(III) chelates represent appealing nanomaterials for the development of dual imaging agents capable to exert contrast both in MRI and nonlinear microscopy. A synthetic route was developed to prepare a lanthanide chelator based on the modification of the tripodal propionate ligand $H_3$ebpatcn with a terminal alkyne-containing homoserine derivative allowing covalent conjugation to **LNO-$N_3$** NPs using azide-alkyne [3 + 2]-cycloaddition. Substitution of the propionate group by a homoserine residue did not affect the coordination capacity of the ligand as indicated by the results of relaxometric measurements on the Gd(III)-chelate **8**. Subsequent click reaction to coated HNPs led to **LNO-Gd** nanoconjugates presenting a homogeneous distribution of Gd(III)-containing complexes at the NP surface with a loading rate of up to $8x10^4$ chelates per NP. The formation of a triazole moiety offers high stability

of the Gd-functionalized HNPs in physiological environment (pH variation, enzymatic cleavage). **LNO-Gd** NPs exhibited strong concentration-dependent contrast enhancement in $T_1$- and $T_2$-weighted images of agarose gel-based phantoms, opening the prospects for dual mode $T_1/T_2$ magnetic contrast formation, as well as intense multi-harmonic signals for cancer cells imaging in the NIR windows. These combined properties highlight the potential of functionalized LNO HNPs to be used as imaging agents in complementary imaging techniques in terms of spatial resolution, penetration depth and sensitivity. In addition to the previously established photo-triggered drug delivery protocols[47,68] and cell tracking capabilities[37,38] of HNP based conjugates, the dual imaging properties herein disclosed enlarge the scope of LNO NPs toward theranostic applications.

## ASSOCIATED CONTENT

**Supporting Information**. The Supporting Information is available free of charge on the ACS Publication website.

Scheme S1

Scheme S2

Scheme S3

Figure S1

Figure S2

Figure S3

Figure S4

Table S1

Table S2

Table S3

Table S4

Table S5

Synthesis protocols for compounds **5**; preparation of **LNO-N$_3$** NPs; Analytical data ($^1$H and $^{13}$C NMR spectra, IR data); TEM images of **LNO** NPs; Surface atomic concentration of **LNO-N$_3$** and **LNO-Gd** NPs measured by XPS; relaxometric properties of **LNO**, **LNO-N$_3$** and **LNO-Gd** NPs.

AUTHOR INFORMATION

**Corresponding Author**

*E-mail: sandrine.gerber@epfl.ch

**Author Contributions**

The manuscript was written through contributions of all authors. RDM designed and performed the functionalization pathways, prepared and characterized the hybrid nanoparticles, contributed to the relaxivity measurements. GC designed, performed and analyzed the multiphoton imaging experiments. AG contributed to the preparation of the hybrid nanoparticles and analyzed the HAADF-STEM images and EDX elemental maps. JV and LN contributed to the development of the synthetic and surface functionalization pathways. KP and IJ prepared the phantom and performed the MRI experiments. FR prepared and characterized the bare LNO nanocrystals under the guidance of YM and RLD. FL, IG, DS and DD contributed to the cell imaging experiments. ASC and MM contributed to the design of the TACN-based chelating ligand. LB and SGL supervised the project, designed the experiments, and prepared the manuscript. All authors have given approval to the final version of the manuscript.

**Funding Sources**

This work was funded by the Interreg V Program (NANOFIMT grant; OncoNanoScreen grant). The multiphoton imaging platform used for the optical measurements was funded by the Swiss National Foundation (R'Equip grant N° 316030-183529).

**Notes**

The authors declare no competing financial interest.

ACKNOWLEDGMENT

The authors thank L. Menin (EPFL ISIC-MSEAP) for her support with MS characterizations, N. Gasilova (EPFL ISIC-MSEAP) for ICP-MS measurements, A. Bornet (EPFL ISIC-NMRP) for his assistance with relaxivity measurements, M. Mensi (EPFL ISIC-XRDSAP) for his support with XPS analyses, the Interdisciplinary Centre for Electron Microscopy (EPFL, CIME) for STEM experiments, S. Ghosh (UniGE, Department of Applied Physics) for her support with multiphoton image acquisition and processing, and S. Kaiser (UNIL, Faculty of Biology and Medicine, Department of Biomedical Sciences) for his support with cell labelling.

REFERENCES

(1) Forbes, S. J.; Rosenthal, N. Preparing the ground for tissue regeneration: from mechanism to therapy. *Nat. Med*. **2014**, *20*, 857-869.

(2) Waldman, A. D.; Fritz, J. M. Lenardo, M. J. A guide to cancer immunotherapy: from T cell basic science to clinical practice. *Nat. Rev. Immunol*. **2020**, *20*, 651-668.

(3) Kircher, M. F.; Gambhir, S. S.; Grimm, J. Noninvasive cell-tracking methods. Nat. Rev. Clin. Oncol. **2011**, *8*, 677-688.

(4) Ni, J. S.; Li, Y.; Yue, W.; Liu, B.; Li, K. Nanoparticle-based Cell Trackers for Biomedical Applications. *Theranostics* **2020**, *10*, 1923-1947.

(5) Kim, J.; Chhour, P.; Hsu, J.; Litt, H. I.; Ferrari, V. A.; Popovtzer, R.; Cormode, D. P. Use of Nanoparticle Contrast Agents for Cell Tracking with Computed Tomography. *Bioconjugate Chem*. **2017**, *28*, 1581-1597.

(6) Sordillo, L. A.; Pu, Y.; Pratavieira, S.; Budansky, Y.; Alfano, R. R. Deep optical imaging of tissue using the second and third near-infrared spectral windows. *J. Biomed. Opt*. **2014**, *19*:056004.

(7) Kobat, D.; Durst, M. E.; Nishimura, N.; Wong, A. W.; Schaffer, C. B.; Xu, C. Deep Tissue Multiphoton Microscopy Using Longer Wavelength Excitation. *Opt. Express* **2009**, *16*, 13354-13364.

(8) Bruns, O. T.; Bischof, T. S.; Harris, D. K.; Franke, D.; Shi, Y.; Riedemann, L. Bartelt, A.; Jaworski, F. B.; Carr, J. A.; Rowlands, C. J.; Wilson, M. W. B.; Chen, O.; Wie, H.; Hwang, G. W.; Montana, D. M.; Coropceanu, I.; Achorn, O. B.; Kloepper, J.; Heeren, J.; So, P. T. C.; Fukumura, D.; Jensen, K. F.; Jain, R. K.; Bawendi, M. G. Next-Generation In Vivo Optical Imaging with Short-Wave Infrared Quantum Dots. *Nat. Biomed. Eng*. **2017**, *1*, 1-11.

(9) Naczynski, D.; Tan, M.; Zevon, M.; Wall, B.; Kohl, J.; Kulesa, A. Chen, S.; Roth, C. M.; Riman, R. E.; Moghe, P. V. Rare-earth-doped biological composites as in vivo shortwave infrared reporters. *Nat. Commun*. **2013**, *4*, 1-10.

(10) Ali, Z.; Abbasi, A. Z.; Zhang, F.; Arosio, P.; Lascialfari, A.; Casula, M. F.; Wenk, A.; Kreyling, W.; Plapper, R.; Seidel, M.; Niessner, R.; Knöll, J.; Seubert, A.; Parak, W. J. Multifunctional Nanoparticles for Dual Imaging. *Anal. Chem*. **2011**, *83*, 2877-2882.

(11) Chen, H.; Zhang, W.; Zhu, G.; Xie, J.; Chen, X. Rethinking Cancer Nanotheranostics. *Nat. Rev. Mater*. **2017**, *2*, 17024.

(12) Stafford, S.; Serrano Garcia, R.; Gun'ko, Y. K. Multimodal Magnetic-Plasmonic Nanoparticles for Biomedical Applications. *Appl. Sci*. **2018**, *8*, 97.

(13) Liu, T.- M.; Conde, J.; Lipińsky, T.; Bednarkiewicz, A. Smart NIR Linear and Nonlinera Optical Nanomaterials for Cancer Theranostics: Prospects in Photomedicine. *Prog. Mater. Sci*. **2017**, *88*, 89-135.

(14) Liu, M.; Anderson, R.- C.; Lan, X.; Conti, P. S.; Chen, K. Recent Advances in the Development of Nanoparticles for Multimodality Imaging and Therapy of Cancer. *Med. Res. Rev*. **2019**, 1-22.

(15) Xu, J.; Gulzar, A.; Yang, D.; Gai, S.; He, F.; Yang, P. Tumor Self-Responsive Upconversion Nanomedicines for Theranostic Applications. *Nanoscale* **2019**, *11*, 17535-17556.

(16) Du, Z.; Gupta, A.; Clarke, C.; Cappadona, M.; Clases, D.; Liu, D.; Yang, Z.; Karan, S.; Price, W. S.; Xu, X. Porous Upconversion Nanostructures as Bimodal Biomedical Imaging Contrast Agents. *J. Phys. Chem. C* **2020**, *124*, 12168-12174.

(17) Norouzi, M. Gold Nanoparticles in Glioma Theranostics. *Pharmacol. Res*. **2020**, *156*, 104753.

(18) Sun, Y.; Yu, M.; Liang, S.; Zhang, Y.; Li, C.; Mou, T.; Yang, W.; Zhang, X.; Li, B.; Huang, C.; Li, F. Fluorine-18 Labeled Rare-Earth Nanoparticles for Positron Emission Tomography (PET) Imaging of Sentinel Lymph Node. *Biomaterials* **2011**, *32*, 2999-3007.

(19) Zhou, J.; Yu, M.; Sun, Y.; Zhang, X.; Zhu, X.; Wu, Z.; Wu, D.; Li, F. Fluorine-18-Labeled $Gd^{3+}/Yb^{3+}/Er^{3+}$ Co-Doped $NaYF_4$ nanophosphors for multimodality PET/MR/UCL imaging. *Biomaterials* **2011**, *32*, 1148-1156.

(20) Ilves, V. G.; Sokovnin, S. Y.; Zuev, M. G.; Uimin, M. A.; Privalova, D. V.; Kozlova, J. Multimodal Upconversion $CaF_2$:Mn/Yr/Er/Si Nanoparticles. *J. Fluor. Chem*. **2020**, *231*, 109457.

(21) Li, H.; Wang, X.; Huang, D.; Chen, G. Recent Advances of Lanthanide-Doped Upconversion Nanoparticles for Biological Applications. *Nanotechnology* **2020**, *31*, 072001.

(22) Sun, Y.; Zhu, X.; Peng, J.; Li, F. Core-Shell Lanthanide Upconversion Nanophosphors as Four-Modal Probes for Tumor Angiogenesis Imaging. *ACS Nano* **2013**, *12*, 11290-11300.

(23) Lee, H.- Y.; Li, Z.; Chen, K.; Hsu, A. R.; Xu, C.; Xie, J.; Sun, S.; Chen, X. PET/MRI Dual-Modality Tumor Imaging Using Arginine-Glycine-Aspertic (RGD)-Conjugated Radiolabeled Iron Oxide Nanoparticles. *J. Nucl. Med*. **2008**, *49*, 1371-1379.

(24) Pillarisetti, S.; Uthaman, S.; Huh, K. M.; Koh, Y. S.; Lee, S.; Park, I.- K. Multimodal Composite Iron Oxide Nanoparticles for Biomedical Applications. *Tissue Eng. Regen. Med*. **2019**, *16*, 451-465.

(25) Hu, D.- H.; Sheng, Z.- H.; Zhang, P.- F.; Yang, D.- Z.; Liu, S.- H.; Gong, P.; Gao, D.- Y.; Fang, S.- T.; Ma, Y.- F.; Cai, L.- T. Hybrid Gold-Gadolinium Nanoclusters for Tumor-Tageted NIRF/CT/MRI Triple-Modal Imaging In Vivo. *Nanoscale* **2013**, *5*, 1624-1328.

(26) Xu, C.; Wang, Y.; Zhang, C.; Jia, Y.; Luo, Y.; Gao, X. AuGd Integrated Nanoprobes for Optical/MRI/CT triple-modal in vivo tumor targeting. *Nanoscale* **2017**, *9*, 4620-4628.

(27) Stasiuk, G. J.; Tamang, S.; Imbert, D.; Poillot, C.; Giardello, M.; Tisseyre, C.; Barbier, E. L.; Fries, P. H.; de Waard, M.; Reiss, P.; Mazzanti, M. Cell-Permeable Ln(III) Chelate-Functionalized InP Quantum Dots as Multimodal Imaging Agents. *ACS Nano* **2011**, *5*, 8193-8201.

(28) Wartenberg, N.; Fries, P.; Raccurt, O.; Guillermo, A.; Imbert, D.; Mazzanti, M. A Gadolinium Complex Confined in Silica Nanoparticles as a Highly Efficient $T_1/T_2$ MRI Contrast Agent. *Chem. Eur. J*. **2013**, *19*, 6980-6983.

(29) Kim, J. S.; Rieter, W. J.; Taylor, K. M. L.; An, H.; Lin, W.; Lin, W. Self-Assembled Hybrid Nanoparticles for Cancer-Specific Multimodal Imaging. *J. Am. Chem. Soc*. **2007**, *129*, 8962-8963.

(30) Albuquerque, G. M.; Souza-Sobrinha, I.; Coiado, S. D.; Santos, B. S.; Fontes, A.; Pereira, G. A. L.; Pereira, G. Quantum Dots and $Gd^{3+}$ Chelates : Advances and Challenges Toward Bimodal Nanoprobes for Magnetic Resonance and Optical Imaging. *Top. Curr. Chem*. **2021**, *379*:12.

(31) Debroye, E.; Parac-Vogt, T. N. Towards Polymetallic Lanthanide Complexes as Dual Contrast Agents for Magnetic Resonance and Optical Imaging. *Chem. Soc. Rev*. **2014**, *43*, 8178-8192.

(32) Dempsey, W. P.; Fraser, S. E.; Pantazis, P. SHG Nanoprobes: Advancing Harmonic Imaging in Biology. *BioEssays* **2012**, *34*, 351-360.

(33) Bonacina, L. Nonlinear Nanomedicine: Harmonic Nanoparticles toward Targeted Diagnosis and Therapy. *Mol. Pharmaceutics* **2013**, *7*, 205-209.

(34) Grange, R.; Lanvin, T.; Hsieh, C.-L.; Pu, Y.; Psaltis, D. Imaging with Second-Harmonic Radiation Probes in Living Tissue. *Biomed. Opt. Express* **2011**, *2*, 2532-2539.

(35) Le Xuan, L.; Zhou, C.; Slablab, A.; Chauvat, D.; Tard, C.; Perruchas, S.; Gacoin, T.; Villela, P.; Roch, J. F. Photostable Second-Harmonic Generation from a Single $KTiOPO_4$ Nanocrystal for Nonlinear Microscopy. *Small* **2008**, *4*, 1332-1336.

(36) Rogov, A.; Irondelle, M.; Ramos-Gomes, F.; Bode, J.; Staedler, D.; Passemard, S.; Courvoisier, S.; Yamamoto, Y.; Waharte, F.; Ciepielewski, D.; Rideau, P.; Gerber-Lemaire, S.; Alves, F.; Salamero, J.; Bonacina, L.; Wolf, J.-P. Simultaneous Multi-Harmonic Imaging of Nanoparticles in Tissues for Increased Selectivity. *ACS Photonics*, **2015**, *2*, 1416-1422.

(37) Dubreil, L.; Leroux, I.; Ledevin, M.; Schleder, C.; Lagalice, L.; Lovo, C.; Fleurisson, R.; Passemard, S.; Kilin, V.; Gerber-Lemaire, S.; Colle, A.M.; Bonacina, L.; Rouger, K. Multi-Harmonic Imaging in the Second Near-Infrared Window of Nanoparticle-Labeled Stem Cells as Effective Monitoring Tool in Tissue Depth. *ACS Nano* **2017**, 11, 6672-6681.

(38) Ramos-Gomes, F.; Möbius, W.; Bonacina, L.; Alves, F.; Markus, M. A. Bismuth Ferrite Second Harmonic Nanoparticles for Pulmonary Macrophage Tracking. *Small* **2019**, *15*, 1803776.

(39) Sugiyama, N.; Sonay, A. Y.; Tussiwand, R.; Cohen, B. E.; Pantazis, P. Effective Labeling of Primary Somatic Stem Cells with $BaTiO_3$ Nanocrystals for Second Harmonic Generation Imaging. *Small* **2018**, *14*, 1703386.

(40) Čulić-Viskota, J.; Dempsey, W. P.; Fraser, S. E.; Pantazis, P. Surface Functionalization of Barium Titanate SHG Nanoprobes for *In Vivo* Imaging in Zebrafish. *Nat. Protoc*. **2012**, *7*, 1618-1633.

(41) Vittadello, L.; Kijatkin, C.; Klene, J.; Dzikonski, D.; Kömpe, K.; Meyer, C.; Paululat, A.; Imlau, M. *In-Vivo* Tracking of Harmonic Nanoparticles: a Study Based on a TIGER Widefield Microscope. *Opt. Mater. Express* **2021**, *11*, 1953-1969.

(42) Vittadello, L.; Klenen, J.; Koempe, K.; Koscor, L.; Szaller, Z.; Imlau, M. NIR-to-NIR Imaging: Extended Excitation Up to 2.2 μm Using Harmonic Nanoparticles with a Tunable hIGh EneRgy (TIGER) Widefield Microscope. *Nanomaterials* **2021**, *11*, 3193.

(43) Madzharova, F.; Nodar, A.; Živanović, V.; Huang, M. R. S.; Koch, C. T.; Esteban, R.; Aizpurua, J.; Kneipp, J. Gold- and Silver-Coated Barium Titanate Nanocomposites as Probes for Two-Photon Multimodal Microspectroscopy. *Adv. Funct. Mater*. **2019**, *29*, 1904289.

(44) Urbain, M.; Riporto, F.; Beauquis, S.; Monnier, V.; Marty, J. –C.; Galez, C.; Durand, C.; Chevolot, Y.; Le Dantec, R.; Mugnier, Y. On the Reaction Pathways and Growth Mechanisms of $LiNbO_3$ Nanocrystals from the Non-Aqueous Solvothermal Alkoxide Route. *Nanomaterials* **2021**, *11*:154.

(45) Nonat, A; Giraud, M.; Gateau, C.; Fries, P. H.; Helm, L.; Mazzanti, M. Gadolinium(III) Complexes of 1,4,7-Triazacyclononane Based Picolinate Ligands: Simultaneous Optimization of Water Exchange Kinetics and Electronic Relaxation. *Dalton Trans*. **2009**, *38*, 8033-8046.

(46) De Matos, R. J. Surface Functionalization of Metal Oxide Harmonic Nanoparticles for Targeted Cancer Imaging. Doctoral dissertation, Ecole Polytechnique Fédérale de Lausanne, Lausanne, 2020.

(47) Vuilleumier, J.; Gaulier, G.; De Matos, R.; Ortiz, D.; Menin, L.; Campargue, G.; Mas, C.; Constant, S.; Le Dantec, R.; Mugnier, Y.; Bonacina, L.; Gerber-Lemaire, S. Two-Photon-Triggered Photorelease of Caged Compounds from Multifunctional Harmonic Nanoparticles. *ACS Appl. Mater. Interfaces*. **2019**, *11*, 27443-27452.

(48) Nonat, A.; Gateau, C.; Fries, P. H.; Mazzanti, M. Lanthanide Complexes of a Picolinate Ligand Derived from 1,4,7-Triazacyclononane with Potential Application in Magnetic Resonance Imaging and Time-Resolved Luminescence Imaging. *Chem. Eur. J*. **2006**, *12*, 7133-7150.

(49) Staedler, D.; Magouroux, T.; Hadli, R.; Joulaud, C.; Extermann, J.; Schwung, S.; Passemard, S.; Kasparian, C.; Clarke, G.; Gerrmann, M.; Le Dantec, R.; Mugnier, Y.; Rytz, D.; Ciepielewski, D.; Galez, C.; Gerber-Lemaire, S.; Juillerat-Jeanneret, L.; Bonacina, L.; Wolf., J.-P. Harmonic

Nanocrystals for Biolabeling: a Survey of Optical Properties and Biocompatibility. *ACS Nano* **2012**, *6*, 2542-2549.

(50) Timpu, F.; Sendra, J.; Renaut, C.; Lang, L.; Timofeeva, M.; Buscaglia, M. T.; Grange, R. Lithium Niobate Nanocubes as Linear and Nonlinear Ultraviolet Mie Resonators. *ACS Photonics* **2019**, *6*, 545-552.

(51) Campargue, G.; La Volpe, L.; Giardina, G.; Gaulier, G.; Lucarini, F.; Gautschi, I.; Le Dantec, R.; Staedler, D.; Diviani, D.; Mugnier, Y.; Wolf, J. –P.; Bonacina, L. Multiorder Nonlinear Mixing in Metal Oxide Nanoparticles. *Nano Lett*. **2020**, *20*, 8725-8732.

(52) Riporto, J.; Urbain, M.; Mugnier, Y.; Multian, V.; Riporto, F.; Bredillet, K.; Beauquis, S.; Galez, C.; Monnier, V.; Chevolot, Y.; Gayvoronsky, V.; Bonacina, L.; Le Dantec, R. Second Harmonic Spectroscopy of ZnO, $BiFeO_3$ and $LiNbO_3$ Nanocrystals. *Opt. Mater. Express* **2019**, *9*, 1955–1966.

(53) Staedler, D.; Passemard, S.; Magouroux, T.; Rogov, A.; Maguire, C. M.; Mohamed, B. M.; Schwung, S.; Rytz, D.; Juestel, T.; Hwu, S.; Mugnier, Y.; Le Dantec, R.; Volkov, Y.; Gerber-Lemaire, S.; Prina-Mello, A.; Bonacina, L.; Wolf, J.-P. Cellular Uptake and Biocompatibility of Bismuth Ferrite Harmonic Advanced Nanoparticles. *Nanomedicine: NBM* **2015**, *11*, 815-824.

(54) Li, J.; Qiu, J.; Guo, W.; Wang, S.; Ma, B.; Mou, X.; Tanes, M.; Jiang, H.; Liu, H. Cellular Internalization of $LiNbO_3$ Nanocrystals for Second Harmonic Imaging and the Effects on Stem Cell Differentiation. *Nanoscale* **2016**, *8*, 7416-7422.

(55) Rohrer, M.; Bauer, H.; Mintorovitch, J.; Requardt, M.; Weinmann, H.- J. Comparison of Magnetic Properties of MRI Contrast Media Solutions at Different Magnetic Field Strengths. *Invest. Radiol*. **2005**, *40*, 715-724.

(56) McDonald, M. A.; Watkin, K. L. Investigations into the Physicochemical Properties of Dextran Small Particulate Gadolinium Oxide Nanoparticles. *Acad. Radiol*. **2006**, *13*, 421-427.

(57) Debouttière, P.-J.; Roux, S.; Vocanson, F.; Billotey, C.; Beuf, O.; Favre-Réguillon, A.; Lin, Y.; Pellet-Rostaing, S.; Lamartine, R.; Perriat, P.; Tillement, O. Design of Gold Nanoparticles for Magnetic Resonance Imaging. *Adv. Funct. Mater*. **2006**, *16*, 2330-2339.

(58) Rieter, W. J.; Kim, J. S.; Taylor, K. M. L.; An, H.; Lin, W.; Tarrant, T.; Lin, W. Hybrid Silica Nanoparticles for Multimodal Imaging. *Angew. Chem. Int. Ed*. **2007**, *46*, 3680-3682.

(59) Tunariu, N.;Blackledge, M.; Messiou, C.; Petralia, G.; Padhani, A.; Curcean, S.; Curcean, A.; Koh, D.- M. What's New for Clinical Whole-Body MRI (WB-MRI) in the 21st Century. *Br. J. Radiol*. **2020**, *93*: 20200562.

(60) Mitchell, M. D.; Kundel, H. L.; Axel, L.; Joseph, P. M. Agarose as a Tissue Equivalent Phantom Materials for NMR imaging. *Magn. Reson. Imaging* **1986**, *4*, 263-266.

(61) Hellerbach, A.; Schuster, V.; Jansen, A.; Sommer, J. MRI Phantoms – Are There Alternatives to Agar? *PLOS One* **2013**, *8*: e70343.

(62) Na, H. B.; Song, I. C.; Hyeon, T. Inorganic Nanoparticles for MRI Contrast Agents. *Adv. Mater*. **2009**, *21*, 2133-2148.

(63) Alipour, A.; Soran-Erdem, Z.; Utkur, M.; Sharma, V. K.; Algin, O.; Saritas, E. U.; Demir, H. V. A New Class of Cubic SPIONs as a Dual-Mode $T_1$ and $T_2$ Contrast Agent for MRI. *Magn. Reson. Imaging* **2018**, *49*, 16-24.

(64) Liu, D.; Li, J.; Wang, C.; An, L.; Lin, J.; Tian, Q.; Yang, S. Ultrasmall Fe@$Fe_3O_4$ Nanoparticles as $T_1$-$T_2$ Dual-Mode MRI Contrast Agents for Targeted Tumor Imaging. *Nanomedicine: NBM* **2021**, *32*, 102335.

(65) Sánchez-Cabezas, S.; Montes-Robles, R.; Gallo, J.; Sancenón, F.; Martinez-Máñez, R. Combining Magnetic Hyperthermia and Dual *T*1/*T*2 MR Imaging Using Highly Versatile Iron Oxide Nanoparticles. *Dalton Trans*. **2019**, *48*, 3883-3892.

(66) Shu, G.; Chen, M.; Song, J.; Xu, X.; Lu, C.; Du, Y.; Xu, M.; Zhao, Z.; Zhu, M.; Fan, X.; Fang, S.; Tang, B.; Dai, Y.; Du, Y.; Ji, J. Sialic Acid-Engineered Mesoporous Polydopamine Nanoparticles Loaded with SPIO and $Fe^{3+}$ as a Novel Theranosthic Agent for T1/T2 Dual-Mode MRI-Guided Combined Chemo-Photothermal Treatment of Hepatic Cancer. *Bioact. Mater*. **2021**, *6*, 1423-1435.

(67) Gao, L.; Yu, J.; Liu, Y.; Zhou, J.; Sun, L.; Wang, J.; Zhu, J.; Peng, H.; Lu, W.; Yu, L.; Yan, Z.; Wang, Y. Tumor-Penetrating Peptide Conjugated and Doxorubicin Loaded $T_1$-$T_2$ Dual Mode MRI Contrast Agents Nanoparticles for Tumor Theranostics. *Theranostics* **2018**, *8*, 92-108.

(68) Vuilleumier, J.; Gaulier, G.; De Matos, R.; Mugnier, Y.; Campargue, G.; Wolf, J.- P.; Bonacina, L.; Gerber-Lemaire, S. Photocontrolled Release of the Anticancer Drug Chlorambucil with Caged Harmonic Nanoparticles. *Helv. Chim. Acta* **2020**, *103*, e1900251.